ROYAL SOCIETY OF CHEMISTRY

PAPER

Check for updates

Achieving efficient near-ultraviolet HLCT emitters *via* isomer engineering

Shuyuan Ge,[a] Yixuan Jiang,[a] Zhuang Cheng,[a] Yi Sak Lee,[b] Xiaoen Shi,[a] Yifu Zhao,[a] Taekyung Kim [ID] *[c] and Ping Lu [ID] *[a]

High-efficiency organic emitters that meet the increasing demand of BT. 2020 for vivid color reproduction are of significant importance for organic light-emitting diodes (OLEDs). In this work, we prepare a series of donor (D)–acceptor (A) type near-ultraviolet (NUV) emitters, **27-TPhCNCZ**, **27-PTPhCNCZ**, **36-TPhCNCZ**, and **36-PTPhCNCZ**, based on benzonitrile, phenyl, and carbazole groups. In toluene solution, **27-TPhCNCZ**, **27-PTPhCNCZ**, **36-TPhCNCZ**, and **36-PTPhCNCZ** exhibit main emission peaks at 374, 389, 384, and 390 nm in the NUV region with high PLQYs over 82%. By varying the substitution site on carbazole (2,7/3,6-positions), the dihedral angles (θ_1/θ_3) between carbazole and neighboring phenyl units and θ_2 between carbazole and benzonitrile are accordingly modulated. Among them, **27-PTPhCNCZ** exhibits LE-dominant hybridized local and charge transfer (HLCT) characteristics compared to the CT-dominant excited states in **27-TPhCNCZ**, **36-TPhCNCZ**, and **36-PTPhCNCZ**. The device based on **27-PTPhCNCZ** realizes the best device performance with an electroluminescence peak at 408 nm, a maximum external quantum efficiency of 7.48%, and CIE coordinates of (0.17, 0.04), matching well with the BT.2020 standard. This work provides reliable guidance for the development of high-efficiency NUV emitters.

Introduction

Organic light-emitting diodes (OLEDs), as an emerging technology for next-generation full-color displays and solid-state lightings, have achieved groundbreaking progress in recent years.[1–3] High-efficiency RGB organic emitters have also made great achievements with the development of OLEDs.[4–7] Nowadays, further extending the emission wavelengths of organic materials has attracted more and more immense research interest for enabling new application scenarios for future OLEDs.[8–10] The ITU-R BT. 2020 standard promulgated by the International Telecommunication Union (ITU) has largely expanded the chromaticity coordinates of primary colors which establishes a wide-gamut color space covering ∼75% of the visible spectrum in the CIE 1931 chromaticity diagram—significantly surpassing conventional sRGB (∼35%) and DCI-P3 (∼53%) standards.[11–15] Near-ultraviolet (NUV) emitters show high potential for reducing the power consumption, broadening the display color gamut of OLEDs, and acting as the host

materials for RGB organic emitters.[16–18] To meet the stringent requirements of ultra-high-definition displays for color fidelity, the strategic advancement of NUV materials underscores the critical scientific and industrial impacts since the refined adjustments in red and green regions have been well achieved.[19,20] There are a number of issues that should be tackled in NUV OLEDs, such as poor color purity, low EL intensity, and the shortage of efficient short-wavelength materials. Therefore, high-quality NUV emitters are being insistently sought yet challenging.

NUV materials normally possess intrinsic wide bandgaps with higher LUMO energy levels and lower HOMO energy levels than conventional materials, which commonly lead to a large carrier injection barrier and decreased carrier combination in the resulting OLEDs.[21,22] To achieve balanced charge injection properties, introduction of electron-donating and electron-withdrawing moieties to construct donor (D)–acceptor (A) type molecules has proved to be an effective solution to address this problem.[23,24] The systematic modulation of the D–A molecular configuration is of significant importance since the dihedral angle between D and A groups serves as a critical structural parameter in governing the distribution of frontier molecular orbitals (FMOs) and excited-state characteristics. For example, D–A type thermally activated delayed fluorescence (TADF) materials feature a strong charge transfer (CT) state with large spatial separation of HOMOs and LUMOs.[25] The minimized

[a] *State Key Laboratory of Supramolecular Structure and Materials, College of Chemistry, Jilin University, 2699 Qianjin Avenue, Changchun 130012, China. E-mail: lup@jlu.edu.cn*

[b] *Department of Information Display, Hongik University, Seoul 04066, Korea*

[c] *Department of Chemical Engineering, Kyung Hee University, Yongin-si, Gyeonggi-do, 17104, Korea. E-mail: taekyung.kim@khu.ac.kr*

This journal is © The Royal Society of Chemistry 2026

J. Mater. Chem. C, 2026, **14**, 4997–5004 | **4997**

overlap between HOMOs and LUMOs commonly affords very small ΔE_{ST} which facilitates the harness of non-radiative triplet excitons through the reverse intersystem crossing (RISC) process from the lowest triplet excited state (T_1) to the lowest singlet excited state (S_1) to achieve 100% exciton utilization efficiency.[26,27] However, excessive D–A distortion (e.g., the D–A dihedral angle is $\approx 90°$) generally reduces the radiative transition dipole moments and causes a bathochromic shift, which severely compromises the color purity and deviates the emission from the NUV region. Reducing the D–A dihedral angle will contribute to enhance the orbital overlap and benefits the hypsochromic shift in the emission spectra.[28] In this regard, D–A type emitters with a hybridized local and charge transfer (HLCT) excited state serve as a good choice for NUV emitters, in which the CT component permits $T_n \rightarrow S_m$ ($m \geq 1$) conversion via reverse intersystem crossing (hRISC) at higher energy levels, whilst the low-lying LE state ensures the emission in the short-wavelength zone.[29–35]

Our prior works reported the molecular design for deep-blue luminogens by rationally modulating the CT and LE components in the excited state by increasing the distance of D/A moieties to improve the oscillator strength and inhibit fluorescence quenching and redshift of emission colors in solid films.[36–40] For fluorescent materials with wider energy gaps, the comprehensive guideline for controlling the excited state characteristics and solid-state state properties still remains insufficient to establish an universal design strategy. In this work, we further design and synthesize a series of hot exciton emitters, **27-TPhCNCZ**, **27-PTPhCNCZ**, **36-TPhCNCZ**, and **36-PTPhCNCZ**, adopting benzonitrile as the acceptor and carbazole as the donor. Through D–A topological engineering, this strategy enables the synchronous ΔE_{ST} modulation as well as maintains partially HOMO/LUMO spatial separation to facilitate the high-lying RISC process. The emission peaks of **27-TPhCNCZ**, **27-PTPhCNCZ**, **36-TPhCNCZ**, and **36-PTPhCNCZ** in toluene solution are observed at 374 nm, 389 nm, 384 nm, and 390 nm located in the NUV region with high PLQYs over 82%. By varying substitution on 2,7 and 3,6-positions of carbazole, the dihedral angles (θ_1/θ_3) between carbazole and neighboring phenyl units and θ_2 between carbazole and benzonitrile are systematically modulated. **27-PTPhCNCZ** achieves the optimal θ_1/θ_3 of 20° and θ_2 of 49° which favors the formation of LE-dominant hybridized local and charge transfer (HLCT) excited states. **27-TPhCNCZ**, **36-TPhCNCZ**, and **36-PTPhCNCZ** with bigger torsion angles of $\theta_1/\theta_2/\theta_3$ all exhibit the CT-dominant excited states. **27-PTPhCNCZ** achieves the best device performance with a maximum external quantum efficiency (EQE_{max}) of 7.48% and CIE coordinates (0.17, 0.04) in the 10 wt% doped device. In contrast, the doped devices based on **27-TPhCNCZ**, **36-TPhCNCZ**, and **36-PTPhCNCZ** exhibit moderate EQE_{max} values (2.71%, 4.38%, and 4.80%, respectively). The magnetic field effect measurement further proves that the highest EQE_{max} in the **27-PTPhCNCZ**-based OLED is primarily ascribed to the hot exciton pathway. This study provides valuable guidance for the investigation of the structure–property relationship of NUV emitters and for the achievement of high-efficiency OLEDs meeting the requirements of the BT. 2020 standard.
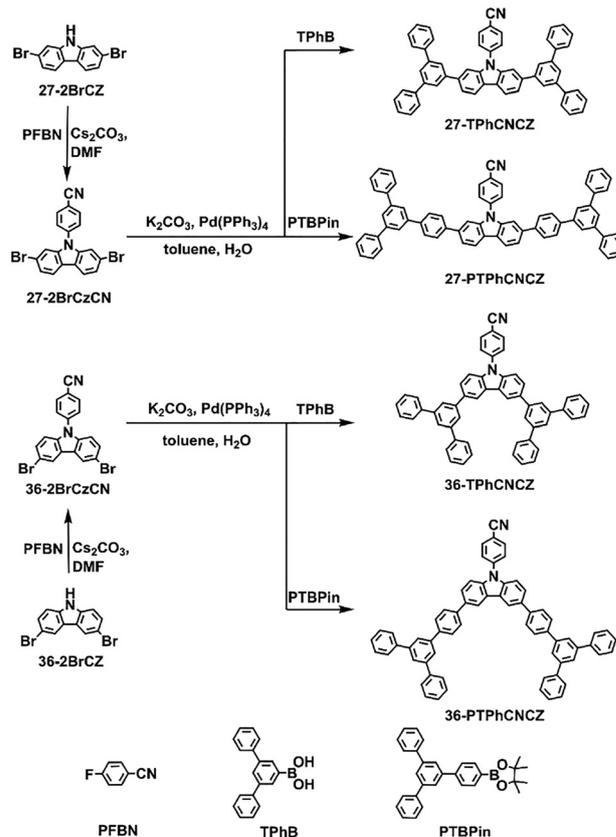

Fig. 1 Synthesis routes to **27-TPhCNCZ**, **27-PTPhCNCZ**, **36-TPhCNCZ**, and **36-PTPhCNCZ**.

Results and discussion

Synthesis and thermal properties

The molecular structures of **27-TPhCNCZ**, **27-PTPhCNCZ**, **36-TPhCNCZ**, and **36-PTPhCNCZ** are shown in Fig. 1. They were facilely prepared in high yields by Suzuki coupling reactions between **TPhB**, **PTBPin**, **27-2BrCzCN**, and **36-2BrCzCN**, respectively.[41] The structural identities of all the compounds were unambiguously confirmed through multinuclear NMR (^{1}H/^{13}C) analysis and high-resolution mass spectrometry, with experimental data consistently matching theoretical predictions. The thermodynamic properties of **27-TPhCNCZ**, **27-PTPhCNCZ**, **36-TPhCNCZ**, and **36-PTPhCNCZ** were characterized by thermogravimetric analysis (TGA) and differential scanning calorimetry (DSC) (Fig. 2 and S13). The glass transition temperature (T_g) was not observed in the DSC test, while **36-TPhCNCZ** displayed a clear exothermic peak which correspond to the crystallization temperature (T_c) of 302 °C. The melting points (T_m) of **27-PTPhCNCZ** and **36-TPhCNCZ** reached 346 °C and 328 °C, respectively. The standard weight loss of 5% (T_d) for **27-TPhCNCZ**, **27-PTPhCNCZ**, **36-TPhCNCZ**, and **36-PTPhCNCZ** were observed to be at 490 °C, 508 °C, 495 °C, and 533 °C, respectively. They all exhibited good thermal stability and could resist thermolysis and the materials' stability was retained during vacuum evaporation. Due to their higher molecular weights, the thermal stabilities of **27-TPhCNCZ**, **27-PTPhCNCZ**, **36-TPhCNCZ**, and **36-PTPhCNCZ** were significantly
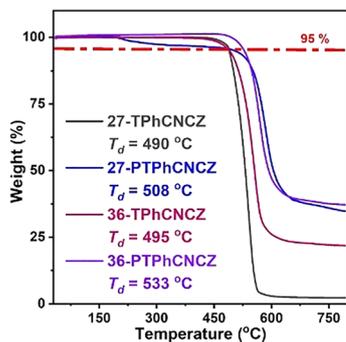
4998 | J. Mater. Chem. C, 2026, **14**, 4997–5004

This journal is © The Royal Society of Chemistry 2026

Fig. 2 TGA curves of **27-TPhCNCZ**, **27-PTPhCNCZ**, **36-TPhCNCZ** and **36-PTPhCNCZ**.

enhanced compared to that of *N*-(benzonitrile)-carbazole (CNCz),[31] which favored their application in OLEDs.

Theoretical calculations and electrochemical properties

The density functional theory (DFT) and time-dependent DFT (TD-DFT) calculations were conducted to elucidate the structure–property relationships of **27-TPhCNCZ**, **27-PTPhCNCZ**, **36-TPhCNCZ**, and **36-PTPhCNCZ** (Fig. 3 and Fig. S14). Among them, **27-TPhCNCZ**, **36-TPhCNCZ**, and **36-PTPhCNCZ** all exhibited similar torsion angles, that is, θ_1 and θ_3 which were between carbazole and neighboring two terphenyl units in **27-TPhCNCZ/36-TPhCNCZ** and two phenyl-terphenyl groups in **36-PTPhCNCZ** were all in the range of 30–39°, and the torsion angle θ_2 which was between benzonitrile and carbazole groups was in the range of 70–76° in these three molecules. The situation was different in **27-PTPhCNCZ**, in which the θ_1/θ_3 were both decreased to 20° and θ_2 was reduced to 49° (Table S1), indicating effective π-conjugation between the carbazole core and adjacent phenyl rings. In all four molecules, the
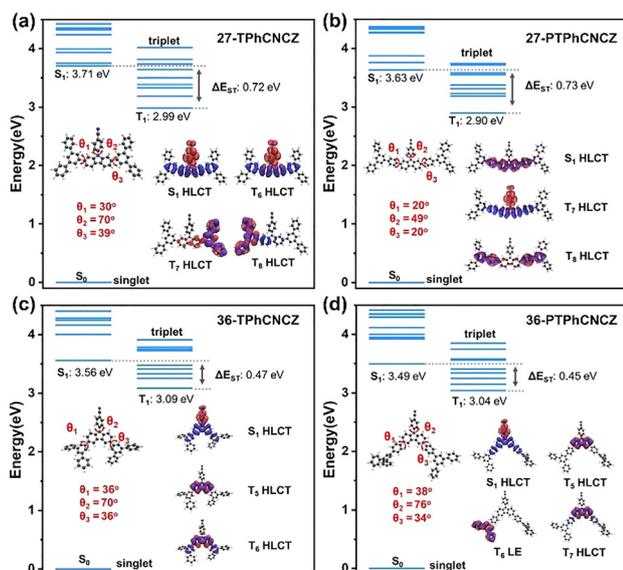
HOMOs are primarily distributed over the electron-rich carbazole units and their adjacent phenyl rings, while the LUMOs are mainly localized on the electron-withdrawing benzonitrile moiety. Notably, the substitution pattern on the carbazole ring plays a critical role in modulating the HOMO distribution. In the 3,6-substituted isomers (**36-TPhCNCZ** and **36-PTPhCNCZ**), the electron density of the HOMO extends toward the benzonitrile group. In contrast, the electronic structure of the HOMO in the 2,7-substituted isomers (**27-TPhCNCZ** and **27-PTPhCNCZ**) more closely resembles that of simple quaterphenyl derivatives (Fig. S15).

To further explore the excited state properties, the natural transition orbitals (NTOs) were calculated and analysed. For the S_1 state, the holes of **27-TPhCNCZ**, **36-TPhCNCZ**, and **36-PTPhCNCZ** were mainly distributed on the carbazole unit and adjacent phenyl units, while the particles were observed to be concentrated on the benzonitrile unit and with some residual on the central carbazole ring, suggesting the CT-dominated HLCT characteristics. In **27-PTPhCNCZ**, the hole and particle of the S_1 state were mainly delocalized on the long-axis skeleton of the whole molecule with high ratio overlap and partial spatial separation, where significant electron density is localized on the carbazole core and adjacent terphenyl moieties, confirming its LE-dominated HLCT characteristics (Fig. 3b). The high-lying T_7/T_8 states of **27-PTPhCNCZ** exhibited the HLCT characteristics similar to the S_1 state which could facilitate the triplet-to-singlet conversion to S_1. It could be seen that the energy difference (ΔE_{ST}) between S_1 and T_1 states was as large as 0.73 eV, which indicated that it was difficult to realize a sufficient RISC from T_1 to S_1. Nevertheless, a small T_7/T_8–S_1 splits ($\Delta E_{S_1T_7}$: 0.05 eV and $\Delta E_{S_1T_8}$: 0.08 eV) could be found, providing the possibility for the RISC process from high-lying triplet energy through a hot exciton channel. The HOMO and LUMO energy levels of **27-TPhCNCZ**, **27-PTPhCNCZ**, **36-TPhCNCZ**, and **36-PTPhCNCZ** were estimated from cyclic voltammetry (Fig. S16). Relative to the ferrocenium/ferrocene (Fc⁺/Fc) redox couple, the oxidation onset potentials of the four compounds were measured at 0.95, 0.98, 0.94, and 0.92 V, respectively. Correspondingly, their reduction onset potentials were recorded at −2.40, −2.35, −2.37, and −2.34 V, a process primarily governed by the electron-accepting benzonitrile unit (Fig. S17). The HOMO/LUMO levels of **27-TPhCNCZ**, **27-PTPhCNCZ**, **36-TPhCNCZ**, and **36-PTPhCNCZ** were calculated to be −5.55/−2.33, −5.58/−2.38, −5.54/−2.36, and −5.52/−2.39 eV, respectively, showing excellent agreement with theoretical predictions. These frontier orbital energy levels provide essential guidance for the rational design of OLED architectures, enabling appropriate energy-level alignment between the emissive layer and adjacent functional layers.

Photophysical properties

The photophysical properties of **27-TPhCNCZ**, **27-PTPhCNCZ**, **36-TPhCNCZ**, and **27-PTPhCNCZ** were systematically investigated to elucidate their excited-state characteristics. As shown in Fig. 5, their absorption spectra in toluene exhibited very similar profiles, indicating a minimal influence of donor substitution positions on the ground-state properties. All compounds

Fig. 3 The ground state geometry and natural transition orbitals (NTOs) of (a) **27-TPhCNCZ**, (b) **27-PTPhCNCZ**, (c) **36-TPhCNCZ** and (d) **36-PTPhCNCZ**, unoccupied (hole) (blue) and occupied (electron) (red).

This journal is © The Royal Society of Chemistry 2026

J. Mater. Chem. C, 2026, **14**, 4997–5004 | **4999**

displayed the main absorption peaks at around 330 nm which was attributed to π–π^* transitions of the phenyl rings and carbazole moieties, and no obvious CT band was observed in toluene. In addition, the measurement of the solvation effect on UV absorption spectra in various solvents with distinct polarities also showed similar absorption spectra in terms of the main peak and profile, and no obvious absorption peak was found even in solvents with high polarity such as acetonitrile (Fig. S18). This observation suggested the little dipolar variations of these emitters for the ground states in different solvents. The large bandgaps of **27-TPhCNCZ**, **27-PTPhCNCZ**, **36-TPhCNCZ**, and **36-PTPhCNCZ** were thus calculated to be 3.34 eV, 3.18 eV, 3.28 eV, and 3.24 eV, respectively, enabling their emission in the NUV region. In toluene solution, the primary emission peaks of **27-TPhCNCZ** and **27-PTPhCNCZ** were observed at 374 nm and 389 nm in the NUV region, respectively, which illustrated that the extra benzene ring and less torsion angles in **27-PTPhCNCZ** led to a higher conjugation length. **36-TPhCNCZ** and **36-PTPhCNCZ** exhibited main emission peaks at 384 nm and 390 nm, suggesting that the phenyl-terphenyl unit at the 3,6-position only induced a little elongation in conjugation degree. Solvatochromic PL experiments (Fig. 4) revealed that **27-TPhCNCZ** and **27-PTPhCNCZ** all displayed fine vibrational structures in all solvents, and the red-shifts of the main emission peaks from hexane to acetonitrile (27 nm for **27-TPhCNCZ** and 8 nm for **27-PTPhCNCZ**) were relatively small. The PLQY values of **27-PTPhCNCZ** were further measured in solvents of different polarity, as summarized in Table S2. As compared, **36-TPhCNCZ** and **36-PTPhCNCZ** only exhibited the fine vibrational structure in hexane and the emission spectra became broadened gradually with the increase of solvent polarity. Moreover, they showed large redshifts of 84 nm for **36-TPhCNCZ** and
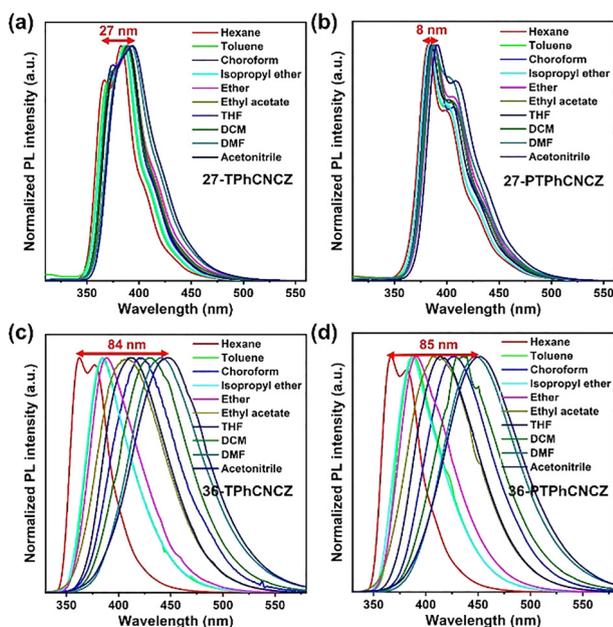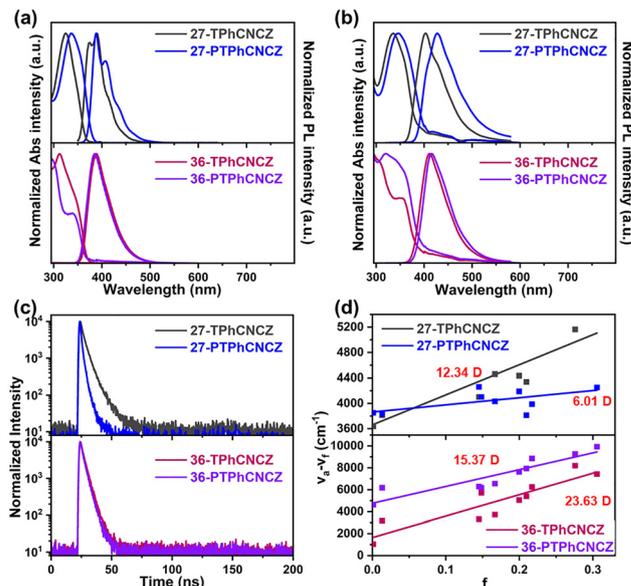

Fig. 5 UV-visible absorption spectra and PL spectra in (a) dilute toluene solutions and (b) thin films. (c) The transient PL decay characteristics. (d) Based on the Lippert–Mataga equation, the linear relationship between the Stokes shift of **27-TPhCNCZ** and **27-TPhCNCZ** and **36-TPhCNCZ** and **36-PTPhCNCZ**.

85 nm for **36-PTPhCNCZ**, confirming the more CT components in the excited state, which was in good accordance with the results from theoretical calculations. Furthermore, the Lippert–Mataga solvatochromic models of the four molecules were measured. As depicted in Fig. 5, **27-TPhCNCZ** showed a good linear relationship with a low excited state dipole moment of 6.01 D, which was the LE-dominated HLCT excited state. The corresponding excited state dipole moments of **27-PTPhCNCZ**, **36-TPhCNCZ**, and **36-PTPhCNCZ** were calculated to be 12.34, 15.37, and 23.63 D, respectively, further confirming the more CT components.

In neat films, intensified intermolecular interactions quenched the fine vibrational structures observed in solution, with emission peaks redshifted to 403 nm (**27-TPhCNCZ**), 428 nm (**27-PTPhCNCZ**), 411 nm (**36-TPhCNCZ**), and 416 nm (**36-PTPhCNCZ**). The solid-state PLQYs were measured as 66.20%, 67.47%, 65.74%, and 69.36%, respectively. The investigation of the AIE activity was also implemented (Fig. S18). The emission intensities of **27-TPhCNCZ**, **27-PTPhCNCZ**, and **36-TPhCNCZ** all enhanced rapidly once f_w exceeded 0%. The intensity became weak when f_w increased to 30%, 50% and 40% for **27-TPhCNCZ**, **27-PTPhCNCZ**, and **36-TPhCNCZ**, respectively, accompanied by slightly red-shifted emission peaks, which could be interpreted by the effect of intermolecular CT.[8] **36-PTPhCNCZ** exhibited attenuated emission intensity with increasing f_w, demonstrating the aggregation-caused quenching effect. Transient PL decay analysis of the films revealed single-exponential lifetimes in the nanosecond regime with no detectable delayed components, indicating rapid S_1 state decay processes for all compounds (Fig. 5c). Based on the peak position of low-temperature fluorescence and phosphorescence spectra, the ΔE_{ST} values for **27-TPhCNCZ**, **27-PTPhCNCZ**, **36-TPhCNCZ**, and **36-PTPhCNCZ** were calculated as 0.80 eV, 0.84 eV, 0.57 eV, and

Fig. 4 Emission spectra of (a) **27-TPhCNCZ**, (b) **27-PTPhCNCZ**, (c) **36-TPhCNCZ**, and (d) **36-PTPhCNCZ** in different polar solvents.

5000 | *J. Mater. Chem. C*, 2026, **14**, 4997–5004

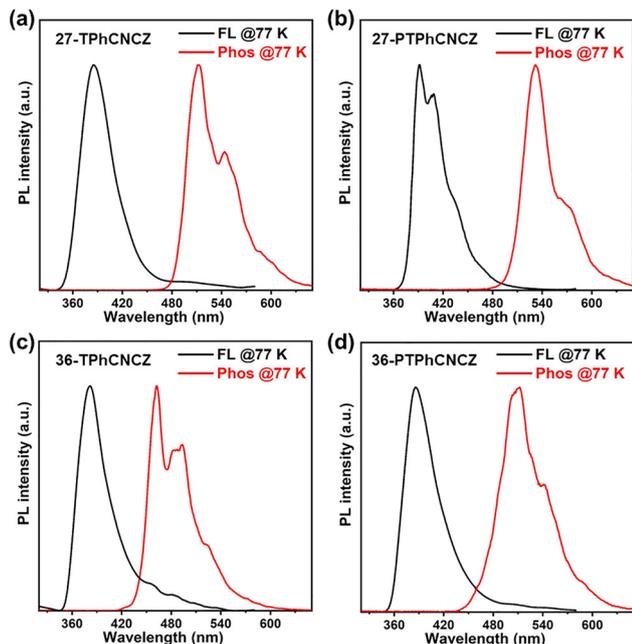This journal is © The Royal Society of Chemistry 2026

Fig. 6 Phosphorescence measurement diagram and PL spectra of (a) **27-TPhCNCZ**, (b) **27-PTPhCNCZ**, (c) **36-TPhCNCZ**, and (d) **36-PTPhCNCZ** in THF (77 K).
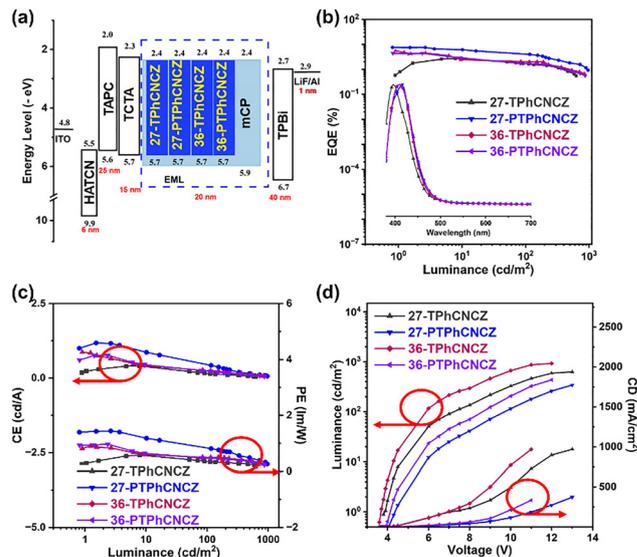

Fig. 7 (a) Energy level diagram of the devices. (b) Normalized EL spectra and EQE *versus* luminance curves, (c) PE–L–CE curves, and (d) J–V–L curves of **27-TPhCNCZ**, **27-PTPhCNCZ**, **36-TPhCNCZ**, and **36-PTPhCNCZ** in the 10 wt% doped OLED.

0.80 eV, respectively (Fig. 6). These large energy gaps unequivocally excluded the involvement of TADF mechanisms. The detailed photophysical parameters are provided in Table 1.

Electroluminescence properties

The doped OLEDs were prepared in order to examine the potentials of **27-TPhCNCZ**, **27-PTPhCNCZ**, **36-TPhCNCZ**, and **36-PTPhCNCZ** as emissive materials for electroluminescence application. After adjusting the functional layers and film thickness, the OLEDs' structures were optimized to be ITO/ HATCN (6 nm)/TAPC (25 nm)/TCTA (15 nm)/emitting layer (EML) (20 nm)/TmPyPb (40 nm)/LiF (1 nm)/Al (120 nm) (EML: mCP:**27-TPhCNCZ**/**27-PTPhCNCZ**/**36-TPhCNCZ**/**36-PTPhCNCZ**, 10 wt%) (Fig. 7a). The turn-on voltages of the four doped OLEDs were all between 3.8 and 3.9 V, indicating a relatively balanced carrier transportation property. The **27-PTPhCNCZ**-based device showed an EL peak at 416 nm with CIE values of (0.17, 0.04), and the maximum external quantum efficiency (EQE_{max}) was

calculated to be 7.48%. **27-TPhCNCZ**, **36-TPhCNCZ**, and **36-PTPhCNCZ**-based OLEDs showed EL spectra peaking at 396 nm, 404 nm, and 408 nm, because of the more confined molecular conjugation length, and the corresponding CIE coordinates were (0.16, 0.03), (0.16, 0.04) and (0.17, 0.04), respectively, which fulfilled with the requirement of BT. 2020. They exhibited moderate EQE_{max}s of 2.70%, 4.80%, and 4.38%, respectively. The EL spectra of the doped OLED based on **27-PTPhCNCZ** under different driving voltages (Fig. S21) remain remarkably stable in both the spectral shape and the peak position, demonstrating excellent spectral stability and reliable color coordinates. This property is beneficial for maintaining color purity in display applications. In this series molecules, adjusting the dihedral angle between the D–A torsion angles yielded optimal device performance, as indicated by the detailed parameters listed in Table 2.

Notably, the optimized device with a maximum external quantum efficiency of **27-PTPhCNCZ** (EQE_{max} = 7.48%) is significantly higher than that of **27-TPhCNCZ** (EQE_{max} = 2.70%). **27-PTPhCNCZ** exhibited an exciton utilization efficiency of over 25% beyond the statistical spin limits. The S_1–T_1 energy gap was evaluated to be

Table 1 Key photophysical properties of **27-TPhCNCZ**, **27-PTPhCNCZ**, **36-TPhCNCZ** and **36-PTPhCNCZ**

Compound	$\lambda_{abs}{}^a$ [nm]		$\lambda_{PL}{}^b$ [nm]		PLQY^c [%]		τ^d [ns]	$k_r{}^e$ [10^7 s^{-1}]	$k_{nr}{}^f$ [10^7 s^{-1}]
	Sol	Film	Sol	Film	Sol	Film			
27-TPhCNCZ	325	335	374	403	84.06	66.20	4.55	14.66	7.32
27-PTPhCNCZ	336	348	389	428	87.68	67.47	2.56	26.36	12.71
36-TPhCNCZ	312	358	384	411	82.34	65.74	3.49	18.84	9.82
36-PTPhCNCZ	339	358	390	416	89.12	69.36	3.23	21.47	9.49

^{a} The UV absorption peaks of toluene solution (10^{-5} M) and the vacuum evaporated neat film at room temperature. ^{b} The main fluorescence emission peaks of toluene solution (10^{-5} M) and the vacuum evaporated neat film at room temperature. ^{c} Absolute PL quantum yields of toluene solution (10^{-5} M) and the neat film estimated by an integrating sphere. ^{d} Fluorescence decay lifetimes of non-doped films. ^{e} Radiation transition rates in non-doped films. ^{f} Non-radiative transition rates in non-doped films.

This journal is © The Royal Society of Chemistry 2026

J. Mater. Chem. C, 2026, **14**, 4997–5004 | **5001**

Table 2 Key performance parameters of 10 wt% doped OLEDs based on **27-TPhCNCZ**, **27-PTPhCNCZ**, **36-TPhCNCZ**, and **36-PTPhCNCZ**

Device	$V_{on}{}^a$ (V)	$L_{max}{}^b$ (cd m^{-2})	$CE_{max}{}^c$ (cd A^{-1})	$PE_{max}{}^d$ (lm W^{-1})	$EQE_{max}{}^e$ (%)	$\lambda_{EL}{}^f$ (nm)	CIE^g (x, y)
27-TPhCNCZ	3.8	627	0.58	0.40	2.70	396	(0.16, 0.03)
27-PTPhCNCZ	3.9	969	1.44	1.22	7.48	416	(0.17, 0.04)
36-TPhCNCZ	3.8	844	0.90	0.74	4.80	404	(0.16, 0.04)
36-PTPhCNCZ	3.9	896	0.97	0.76	4.38	408	(0.17, 0.04)

^{a} Turn-on voltage at 1 cd m^{-2}. ^{b} Maximum brightness. ^{c} Maximum current efficiency. ^{d} Maximum power efficiency. ^{e} The maximum external quantum efficiency. ^{f} The EL emission peak of the EL spectrum at 100 cd m^{-2}. ^{g} Color coordinates at 100 cd m^{-2}.

0.73 eV in theoretical calculations and thus the RISC process from T_1 to hinder the ISC process of $T_n \rightarrow T_1$ contributed to a relatively lower accumulation of T_1 excitons, which could largely restrain the triplet–triplet annihilation triggered by long-lived T_1 excitons (Fig. 8). This clarifies that S_1 was notable to occur efficaciously, suggesting that the TADF process can be completely excluded. The NTOs characteristics of HLCT feature and small energy gaps (0.05 and 0.09 eV) between T_7 (3.58 eV), T_8 (3.72 eV) and S_1 (3.63 eV) could benefit the RISC process from $T_7 \rightarrow S_1$ and $T_8 \rightarrow S_1$. The magnetic field effect (MFE) provides an effective approach for probing spin-transition processes between singlet and triplet excitons. Unlike singlet states, triplet excitons possess a nonzero magnetic moment, allowing an external magnetic field to induce spin mixing between the singlet and triplet manifolds. As spin-dependent processes, both hRISC and triplet–triplet fusion (TTF) yield distinct magneto-electroluminescence (MEL) responses. Monitoring the variation in EL intensity with a magnetic field thus offers an indirect route to investigate triplet exciton dynamics.[42–44] The MEL characteristics of both devices were completely different from those of TTF-based devices. The MEL responses of both devices exhibit three notable characteristics: (i) a rapid increase in MEL intensity within the low-field regime (0–50 mT), (ii) saturation behavior at elevated magnetic fields, and (iii) a positive correlation between MEL amplitude and applied current density. These observations are indicative of magnetic field-induced perturbation of ISC and RISC rates between singlet and triplet manifolds, particularly within the polaron-pair state and high-lying excited states, consistent with behavior reported in HLCT-based OLEDs.[45,46]

According to the mechanism proposed by Bin Hu *et al.*, magnetic fields lift the triplet spin degeneracy by modifying the sublevel population, enabling energetic intersection of singlet and triplet states and promoting triplet-to-singlet transitions via spin-mixing pathways.[47] The origin of MEL in both devices was attributed to singlet–triplet interconversion occurring within high-lying excited states rather than the lowest excitonic states. The observed current density dependence was explained by an increase in the triplet population in polaron-pair/high-lying states, thus enhancing the up-conversion efficiency to singlets. Both materials exhibited a positive magnetic field high-order triplet energy levels (T_n, $n \geq 2$) which were activated by the external magnetic field, and the reverse interband transitions through the hRISC channel enhanced the density of singlet excitons. A slight negative slope of the MEL signal in the high magnetic field region (50–300 mT) at high current density (30 mA cm^{-2}) in the **27-TPhCNCZ** device indicated that small number of singlets were converted through TTF processes.[48] Collectively, these findings confirmed that LE-dominant HLCT-mediated triplet harvesting was the dominant exciton conversion pathway in **27-PTPhCNCZ** devices and the exciton distribution could be controlled by matching the donor–acceptor energy levels through the spin-dependent tunnelling process, providing a new strategy for developing high-efficiency NUV OLED devices.

Conclusions

In summary, four NUV materials, **27-TPhCNCZ**, **27-PTPhCNCZ**, **36-TPhCNCZ** and **36-PTPhCNCZ**, are designed and successfully synthesized. Through a conjugation-extension strategy, the dihedral angles between the carbazole core and the adjacent two phenyl units (θ_1/θ_3) as well as between the benzonitrile acceptor and the carbazole donor (θ_2) were systematically modulated, enabling the variation in molecular excited-state characteristics. Among them, **27-PTPhCNCZ** exhibits a LE-dominant HLCT state, whereas **27-TPhCNCZ**, **36-TPhCNCZ**, and **36-PTPhCNCZ** all display CT-dominant excited-state features. **27-TPhCNCZ**, **27-PTPhCNCZ**, **36-TPhCNCZ** and **36-PTPhCNCZ** display main emission peaks at 374 nm, 389 nm, 384 nm and 390 nm and PLQYs of 84.06%, 87.68%, 82.34%, and 89.12% in toluene solution, respectively. Notably, the doped OLED based on **27-PTPhCNCZ** achieves the best device performance with an EQE$_{max}$ of 7.48% at CIE (0.17, 0.04). Combining the results of computational simulations, the analysis of photophysical properties, and the magnetic field effect measurement, the highest EQE$_{max}$ and higher exciton utilization efficiency in the **27-PTPhCNCZ**-based OLED are primarily ascribed to the hot exciton pathway. This work provides reliable guidance for the development of high-efficiency NUV emitters matching the BT.2020 standard.
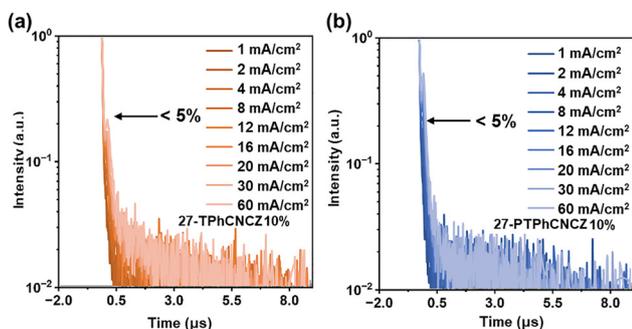

Fig. 8 The transient EL decay curves of doped OLEDs based on (a) **27-TPhCNCZ**, and (b) **27-PTPhCNCZ** at different current densities.

5002 | *J. Mater. Chem. C*, 2026, **14**, 4997–5004

This journal is © The Royal Society of Chemistry 2026

Author contributions

Shuyuan Ge: conceptualization, data curation, formal analysis, investigation, methodology, project administration, validation, and writing – original draft. Yixuan Jiang: supervision. Zhuang Cheng: supervision. Yi Sak Lee: supervision, investigation, data curation, and writing – review and editing. Xiaoen Shi: supervision. Yifu Zhao: supervision. Taekyung Kim: supervision. Ping Lu: conceptualization, data curation, funding acquisition, resources, supervision, validation, and writing – review and editing.

Conflicts of interest

There are no conflicts to declare.

Data availability

The data supporting this article have been included as part of the supplementary information (SI). Supplementary information: general information, photophysical properties, and device characterization. See DOI: https://doi.org/10.1039/d5tc04185f

Acknowledgements

References

1 C. W. Tang and S. A. VanSlyke, *Appl. Phys. Lett.*, 1987, **51**, 913–915.
2 V. Jankus, C. J. Chiang, F. Dias and A. P. Monkman, *Adv. Mater.*, 2013, **25**, 1455–1459.
3 F. Zhan, K. Xu, T. Tsuboi, Y. She and G. Li, *Angew. Chem., Int. Ed.*, 2025, **64**, e202505328.
4 M. Zhu and C. Yang, *Chem. Soc. Rev.*, 2013, **42**, 4963–4976.
5 J. Chen, H. Liu, J. Guo, J. Wang, N. Qiu, S. Xiao, J. Chi, D. Yang, D. Ma, Z. Zhao and B. Z. Tang, *Angew. Chem., Int. Ed.*, 2022, **61**, e202116810.
6 C. Du, H. Liu, Z. Cheng, S. Zhang, Z. Qu, D. Yang, X. Qiao, Z. Zhao and P. Lu, *Adv. Funct. Mater.*, 2023, **33**, 2304854.
7 Z. Cheng, C. Du, S. Ge, Y. Wang, F. Liu, Y. Chang, Y. Lv and P. Lu, *Chem. Eng. J.*, 2023, **474**, 145867.
8 H. Chen, T. Fan, G. Zhao, D. Zhang, G. Li, W. Jiang, L. Duan and Y. Zhang, *Angew. Chem., Int. Ed.*, 2023, **62**, e202300934.
9 J. Jin, C. Duan, H. Jiang, P. Tao, H. Xu and W. Y. Wong, *Angew. Chem., Int. Ed.*, 2023, **62**, e202218947.
10 Y. J. Yu, Z. Q. Feng, X. Y. Meng, L. Chen, F. M. Liu, S. Y. Yang, D. Y. Zhou, L. S. Liao and Z. Q. Jiang, *Angew. Chem., Int. Ed.*, 2023, **62**, e202310047.
11 M. Sugawara, S. Y. Choi and D. Wood, *IEEE. Signal. Process. Mag.*, 2014, **31**, 170–174.
12 B. Bryce-Smith, *Photochemistry*, 1961, **7**, 1–458.
13 J. Zhao, B. Liu, Z. Wang, Q. Tong, X. Du, C. Zheng, H. Lin, S. Tao and X. Zhang, *ACS Appl. Mater. Interfaces*, 2018, **10**, 9629–9637.
14 W. Li, Y. Pan, R. Xiao, Q. Peng, S. Zhang, D. Ma, F. Li, F. Shen, Y. Wang, B. Yang and Y. Ma, *Adv. Funct. Mater.*, 2014, **24**, 1609–1614.
15 C. Liao, S. Wang, B. Chen, Q. Xie, J. Feng, J. Bai, X. Li and H. Liu, *Angew. Chem., Int. Ed.*, 2024, **64**, e202414905.
16 G. Li, B. Li, H. Zhang, X. Guo, C. Lin, K. Chen, Z. Wang, D. Ma and B. Z. Tang, *ACS Appl. Mater. Interfaces*, 2022, **14**, 10627–10636.
17 S. Zeng, C. Xiao, J. Zhou, Q. Dong, Q. Li, J. Lim, H. Ma, J. Y. Lee, W. Zhu and Y. Wang, *Adv. Funct. Mater.*, 2022, **32**, 2113183.
18 H. Huang, R. Chen, S. He, S. Wang, H. Qi, L. Peng, Y. Liu, S. Ying and S. Yan, *Dyes Pigm.*, 2024, **231**, 112420.
19 J. Lou, G. Li, X. Guo, B. Li, D. Yang, H. Zhang, Z. Wang and B. Z. Tang, *Small*, 2023, **20**, 2308468.
20 S. Wang, J. Zhou, J. Jin, H. Jiang, M. Mai, L. Duan, X. Zhang and W. Y. Wong, *ACS Appl. Mater. Interfaces*, 2025, **17**, 31192–31200.
21 S. Zhang, L. Yao, Q. Peng, W. Li, Y. Pan, R. Xiao, Y. Gao, C. Gu, Z. Wang, P. Lu, F. Li, S. Su, B. Yang and Y. Ma, *Adv. Funct. Mater.*, 2015, **25**, 1755–1762.
22 J. Jayabharathi, A. Prabhakaran, V. Thanikachalam and M. Sundharesan, *RSC Adv.*, 2016, **6**, 62208–62217.
23 B. Chen, B. Liu, J. Zeng, H. Nie, Y. Xiong, J. Zou, H. Ning, Z. Wang, Z. Zhao and B. Z. Tang, *Adv. Funct. Mater.*, 2018, **28**, 1803369.
24 R. Guo, W. Liu, S. Ying, Y. Xu, Y. Wen, Y. Wang, D. Hu, X. Qiao, B. Yang, D. Ma and L. Wang, *Sci. Bull.*, 2021, **66**, 2090–2098.
25 T. Hua, Y. C. Liu, C. W. Huang, N. Li, C. Zhou, Z. Huang, X. Cao, C. C. Wu and C. Yang, *Chem. Eng. J.*, 2022, **433**, 133598.
26 B. Ren, C. Zuo, Y. Sun and L. Ding, *J. Semicond.*, 2021, **42**, 050201.
27 B. Li, G. Tang, L. Zhou, D. Wu, J. Lan, L. Zhou, Z. Lu and J. You, *Adv. Funct. Mater.*, 2017, **27**, 1605245.
28 A. Khan, F. C. Kong, J. Kazmi, S. Kumar, T. Leydecker and Z. Wang, *J. Mater. Chem. C*, 2025, **13**, 5624–5632.
29 F. Lucas, D. Medina-Lopez, C. Banga-Kpako, T. T. Huynh, J. S. Lauret and S. Campidelli, *ACS Appl. Nano Mater.*, 2025, **8**, 8473–8479.
30 X. Tang, Q. Bai, T. Shan, J. Li, Y. Gao, F. Liu, H. Liu, Q. Peng, B. Yang, F. Li and P. Lu, *Adv. Funct. Mater.*, 2018, **28**, 1705813.
31 X. Qian, F. Chu, W. Zhou, Z. Zheng, X. Chen and Y. Zhao, *J. Phys. Chem. Lett.*, 2023, **14**, 3335–3342.
32 Z. Zhang, C. L. Chen, Y. A. Chen, Y. C. Wei, J. Su, H. Tian and P. T. Chou, *Angew. Chem., Int. Ed.*, 2018, **57**, 9880–9884.
33 H. Zhang, G. Li, X. Guo, K. Zhang, B. Zhang, X. Guo, Y. Li, J. Fan, Z. Wang, D. Ma and B. Z. Tang, *Angew. Chem., Int. Ed.*, 2021, **60**, 22241–22247.
34 Q. Xie, C. Liao, H. Liu, S. Wang and X. Li, *J. Mater. Chem. C*, 2024, **12**, 11085–11093.
35 J. Lei, Y. K. Chen, M. J. Wang, C. L. Ko, W. Y. Hung, L. Y. Hsu, T. L. Wu and C. H. Cheng, *ACS Mater. Lett.*, 2025, **7**, 1896–1904.

This journal is © The Royal Society of Chemistry 2026

J. Mater. Chem. C, 2026, **14**, 4997–5004 | **5003**

36 Z. Cheng, X. He, H. Liu, S. Ge, Y. Jiang, F. Liu and P. Lu, *J. Mater. Chem. C*, 2025, **13**, 2508–2516.

37 L. Yao, S. Zhang, R. Wang, W. Li, F. Shen, B. Yang and Y. Ma, *Angew. Chem., Int. Ed.*, 2014, **53**, 2119–2123.

38 D. Zhong, X. Yang, X. Deng, X. Chen, Y. Sun, P. Tao, Z. Li, J. Zhang, G. Zhou and W. Y. Wong, *Chem. Eng. J.*, 2023, **452**, 139480.

39 Y. Sun, D. Zhong, S. Liu, L. Yue, Z. Feng, X. Deng, X. Chen, X. Yang and G. Zhou, *J. Mater. Chem. C*, 2023, **11**, 4694–4702.

40 D. Zhong, R. Zhu, J. Zhang, P. Tao, B. Su, X. Yang, Y. Sun, L. Yue, G. Zhou and W. Y. Wong, *Chem. Sci.*, 2025, **16**, 17156–17164.

41 B. Ma, B. Zhang, H. Zhang, Y. Huang, L. Liu, B. Wang, D. Yang, D. Ma, B. Z. Tang and Z. Wang, *Adv. Sci.*, 2024, **11**, 2407254.

42 K. J. Kim, J. Kim, J. T. Lim, J. Heo, B. J. Park, H. Nam, H. Choi, S. S. Yoon, W. Kim, S. Kang and T. Kim, *Mater. Horiz.*, 2024, **11**, 1484–1494.

43 L. Zhang, D. Hu, S. Wang and Y. Ma, *J. Lumin.*, 2024, **273**, 120696.

44 H. Lee and T. Kim, *ACS Appl. Mater. Interfaces*, 2024, **16**, 26468–26477.

45 Y. Xu, X. Liang, X. Zhou, P. Yuan, J. Zhou, C. Wang, B. Li, D. Hu, X. Qiao, X. Jiang, L. Liu, S. J. Su, D. Ma and Y. Ma, *Adv. Mater.*, 2019, **31**, 1807388.

46 K. P. Patel, H. Lee, S. C. Kim, Y. Jeong, T. Kim and J. Y. Lee, *Dyes Pigm.*, 2023, **219**, 111504.

47 B. Hu, L. Yan and M. Shao, *Adv. Mater.*, 2009, **21**, 1500–1516.

48 H. Lee, V. V. Patil, J. Lim, B. K. Min, Y. M. Rhee, Y. K. Kim, T. Kim and J. Y. Lee, *Adv. Opt. Mater.*, 2022, **10**, 2200256.